Application of Feature Tracking Using K-Nearest-Neighbor Vector Field Consensus in Sea Ice Tracking

Bin He ⓘ, Xi Zhao, Ying Chen, Chuang Liu ⓘ, and Xiaoping Pang ⓘ

Abstract—A feature-tracking algorithm algorithm utilizing the proposed *K*-nearest-neighbor vector field consensus (KVFC) to filter outliers is developed to monitor the dynamic changes of sea ice retrieval from synthetic aperture radar (SAR) images. The KVFC is based on vector field consensus and combines with local neighborhood correspondences to optimize the elimination of outliers while retaining inliers as many as possible. The proposed KVFC was evaluated and compared with several algorithms on three standard datasets and Sentinel-1 image pairs in the Fram Strait and the Beaufort Sea. The KVFC obtained more sea-ice drift vectors than the nearest neighbor similarity ratio (NNSR) with a 0.7 threshold and generated dense distribution of sea-ice drift vectors combined with the HH and HV channels. Using buoy datasets to calculate the sea-ice drift speed and evaluate algorithm performance, the proposed approach yielded a lower mean error (KVFC: -0.150 cm/s, NNSR: 0.407 cm/s), lower root mean square error (KVFC: 0.476 cm/s, NNSR: 1.817 cm/s), and lower angle deviation (KVFC: 3.542°, NNSR: 10.318°) compared to the NNSR.

Index Terms—Correspondences, feature, *K*-nearest-neighbor vector field consensus (KVFC), sea-ice drift, synthetic aperture radar (SAR).

I. INTRODUCTION

SEA-ICE drift refers to the speed and direction of sea-ice motion and is an important factor in sea-ice change. Kwok *et al.* [1] confirmed that in the Arctic, sea-ice drift speed has been increasing over a long time, requiring greater attention and further exploration. There are many drivers causing variations of sea-ice drift, such as thickness, concentration, and surface wind stress [2], making estimation more complicated and challenging. Monitoring sea-ice drift is crucial in numerous fields. For example, Nakata *et al.* [3] obtained sea-ice velocity estimated from AMSR-E data, which they then used in a simplified polynya model to calculate ice production and help understand the mechanism of the polynya. Spatial changes in sea ice affect the exchange of salt and heat in the ocean [4]. Sea-ice drift can be used to study the volume of sea-ice export [5], [6] and develop safe navigation routes that help sea vessels avoid sea ice. These applications indicate the importance of studying sea-ice drift.

At the end of the 19th century, ship observations were used to measure sea-ice speed [7]. Later, buoys were used to obtain time and position information in monitoring sea-ice dynamics. With the development of remote sensing technology, satellite images have been utilized in large-scale ice drift monitoring. In recent years, various properties of sea ice have been estimated and analyzed using synthetic aperture radar (SAR) due to its high temporal resolution and extensive spatial coverage [8]–[13]. Various methods have been proposed and developed calculating sea-ice motion using SAR data.

Many algorithms have been developed to estimate sea-ice drift [14]–[22]. The feature-tracking algorithm detects a set of keypoints from two images and finds the correspondence between them to obtain sea ice offset. Muckenhuber *et al.* [24] used oriented FAST and rotated BRIEF (ORB) [23] to extract keypoints and adjusted several parameters to make the algorithm suitable for tracking sea-ice drift. Demchev *et al.* [25] applied accelerated-KAZE features on Sentinel-1 images, showing the benefits of nonlinear multiscale image representations. Suganya *et al.*[26] adopted a similar method and integrated phase correlation. While monitoring sea-ice drift has significantly improved, finding good quality correspondences remains challenging [27]. Many researchers use nearest neighbor similarity ratio (NNSR) [28] with a strict threshold to remove outliers that imply wrong correspondences. However, a strict threshold value also filters out a large number of inliers that provide correct drift positions and thus hampers to generate global sea-ice drift products. New techniques in sea-ice drift estimation should be developed, removing as many outliers as possible while increasing the number of inliers.

In this study, we developed a *K*-nearest-neighbor vector field consensus (KVFC) algorithm for point-to-point correspondences to improve the performance of screening correspondences. The proposed KVFC approach is developed based on the vector field consensus (VFC) algorithm, which learns a vector field from sparse correspondences [29]. Compared with VFC, KVFC adds a local information weight to each Gaussian mixture model (GMM) component to generate more quality

Fig. 1.   Several image pairs from (a) Dataset I, (b) Dataset II, and (c) Dataset III.

correspondences. KVFC considers the coherence of sea-ice drift, encourages the mining of inliers, and suppresses outliers in the vector sparse area, to achieve better results than NNSR with a strict threshold.

The rest of this article is organized as follows. Section II introduces the data used in the experiments, and Section III discusses details of sea ice tracking and introduces the KVFC. In Section IV, we present the results of the experiments, including the parameter tuning, comparison of filtering correspondences algorithms, comparison of different polarizations, computational efficiency, and validation. The discussion of results is provided in Section V. Finally, Section VI concludes this article.

II. Data

The following two datasets were used in this study: 1) standard datasets in computer science to test the performance of KVFC and compare with other algorithms; 2) SAR image pairs to show the application of KVFC in real-sea-ice drift cases.

A. Data for Testing KVFC

The data used for testing the performance of KVFC consist of three datasets, VGG (Dataset I) [30], Symbench (Dataset II) [31], and AdelaideRMF (Dataset III) [32], which are composed of 40, 46, and 38 image pairs, respectively. These datasets contain different changes, including rotation, multistructures, zoom, light change, and viewpoint change. We assessed whether the correspondences found in each image pair were inliers based on each homography matrix H in Datasets I and II. For Dataset III, the correspondences did not have to be classified because the inliers and outliers have been manually labeled. Some sample image pairs are shown in Fig. 1.

B. Data for Sea Ice Tracking

The Sentinel-1 satellite is an earth observation satellite of the Global Monitoring for Environment and Security executed by the European Space Agency. It consists of Sentinel-1A and Sentinel-1B, both carrying a *C*-band SAR. The satellites are particularly useful in studying the polar regions given its advantage of having two satellites operating simultaneously. The ''Extra-wide Swath Mode Ground Range Detected with Medium Resolution'' mode was used in this study, covering an area of 400 km x 400 km with a pixel resolution of 40 m x 40 m. Three pairs of raw images were selected as the demonstration set to analyze algorithms and another 20 image pairs in these areas were used for testing (see Table I).

We first processed radiometric calibration by calculating the normalized radar cross-section σ_{raw}^0 using the equation

$$\sigma_{\mathrm{raw}}^0 = \frac{\mathrm{DN}_i^2}{A_i^2} \tag{1}$$

where i represents the ith pixel, and DN_i and A_i are the digital number and the value of the normalization coefficient from Sentinel-1 data files. Because HV polarization has significant thermal noise, the HV polarization data are denoised. Geocoding was then carried out, and the projection was changed to stereographic. We cropped the common rectangular area in each image pair as the research areas. Finally, a down-scaling strategy was adopted to resample the image pixel to 80 m × 80 m, reducing noise interference and improving computational efficiency [33].

Using buoy data is a good way to test the performance of the sea ice tracking. The International Arctic Buoy Programme (IABP) was established in 1978 based on the recommendation of the U.S. National Academy of Sciences in 1974 to build a network of buoys for monitoring sea level pressure, surface air temperature, and sea-ice motion in the Arctic [34]. At the end of the experiment, according to the selected times and areas of Sentinel-1 images, we selected the nearest 20 buoys from the IABP to evaluate the performance of our proposed algorithm. Fig. 2 shows the location of our selected buoys and testing image pairs.

III. Method

To obtain the final sea-ice drift images, a number of complex processing steps had to be undertaken. These steps could be grouped into the following three stages:

1) keypoints detection and matching;
2) elimination of outliers;
3) sea-ice drift product generation.

Fig. 3 presents the flowchart detailing the sea-ice tracking framework.

A. Keypoints Detection and Matching

Before applying a detector to identify the keypoints, each image pixel has to be normalized to a value range of 0–255.

Given two processed SAR images (I, I'), keypoints and local feature descriptors in each image are obtained through a detector–descriptor combination. Currently, many developed methods are available dealing with this in computer vision, e.g., scale invariant feature transform (SIFT), speeded-up robust features [35], and ORB. For this study, we used the ORB algorithm to achieve keypoints detection and matching.

TABLE I
INFORMATION OF SENTINEL-1 SAR IMAGES PAIRS

No	Region	First image acquisition time	Second image acquisition time	Time gap	Polarization
Case 1	Fram Strait	28-MAY-2020 08:01:01	29-MAY-2020 07:53:41	24 h	HH + HV
Case 2	Beaufort Sea	19-SEP-2020 17:04:50	21-SEP-2020 16:48:24	48 h	HH + HV
Case 3	Beaufort Sea	12-OCT-2020 16:24:53	14-OCT-2020 16:08:33	48 h	HH + HV
Case 4	Beaufort Sea	05-OCT-2019 16:33:10	06-OCT-2019 16:23:47	24 h	HH + HV
Case 5	Beaufort Sea	07-NOV-2020 16:05:33	08-NOV-2020 15:08:16	24 h	HH + HV
Case 6	Fram Strait	14-OCT-2020 07:51:59	16-OCT-2020 07:35:39	48 h	HH + HV
Case 7	Central Arctic	16-JAN-2021 14:42:57	18-JAN-2021 14:26:37	48 h	HH + HV
Case 8	Beaufort Sea	09-NOV-2021 15:59:27	11-NOV-2021 16:32:17	48 h	HH + HV
Case 9	Central Arctic	19-OCT-2021 14:44:06	21-OCT-2021 14:27:46	48 h	HH + HV
Case 10	Central Arctic	18-OCT-2021 14:03:15	19-OCT-2021 14:44:06	24 h	HH + HV
Case 11	Beaufort Sea	09-JAN-2021 15:44:53	10-JAN-2021 15:35:48	24 h	HH + HV
Case 12	Beaufort Sea	08-OCT-2021 17:55:41	09-OCT-2021 17:46:54	24 h	HH + HV
Case 13	Beaufort Sea	21-AUG-2018 18:27:11	22-AUG-2018 18:18:12	24 h	HH + HV
Case 14	Central Arctic	15-AUG-2021 07:59:07	16-AUG-2021 08:39:58	24 h	HH + HV
Case 15	Central Arctic	12-OCT-2019 05:38:14	14-OCT-2019 05:21:54	48 h	HH + HV
Case 16	Central Arctic	11-DEC-2021 03:19:31	13-DEC-2021 03:03:11	48 h	HH + HV
Case 17	Central Arctic	12-DEC-2021 04:00:22	13-DEC-2021 03:03:11	24 h	HH + HV
Case 18	Beaufort Sea	03-FEB-2021 18:02:39	04-FEB-2021 17:53:51	24 h	HH + HV
Case 19	Central Arctic	04-SEP-2021 01:56:15	06-SEP-2021 01:39:55	48 h	HH + HV
Case 20	Beaufort Sea	10-JAN-2021 15:35:48	11-JAN-2021 15:28:24	24 h	HH + HV
Case 21	Fram Strait	30-DEC-2020 08:01:05	01-JAN-2021 07:44:39	48 h	HH + HV
Case 22	Central Arctic	15-NOV-2020 14:58:03	16-NOV-2020 15:38:55	24 h	HH + HV
Case 23	Central Arctic	16-NOV-2020 15:38:55	17-NOV-2020 14:41:56	24 h	HH + HV

In the ORB algorithm, FAST-9 detector and rBRIEF descriptor need to be executed. FAST-9 detector [36] is used to detect keypoints. First, a pixel is selected and assumes its intensity to be I_p. To determine whether the pixel is a keypoint, a threshold $t_{\text{different}}$ is first established. When the absolute value of the difference between the intensity of two pixels is greater than $t_{\text{different}}$, the two pixels are considered to be different. The 16 pixels around the selected pixel are also taken into consideration. I_p is recognized as a keypoint if nine consecutive pixels are different from it. The top N_{kp} keypoints are picked from the keypoints ordered using a Harris corner measure [37]. ORB has the rotational invariance by adding the orientation of each keypoint. As a descriptor, rBRIEF is a modified version of BRIEF and is applied to describe the keypoints. A good subset of binary tests is chosen using Rublee *et al.* [23] and combined with the orientation to calculate the local feature descriptor.

Finally, the keypoints of the two images are matched based on the feature similarity. The Hamming distance is then used as a basis in measuring the similarity of feature vectors.

B. Elimination of Outliers

At the elimination of outlier phase, NNSR is used to perform prefiltering on the correspondences. However, NNSR does not take into account the nature of sea-ice motion coherence, a lot of outliers left may lead to an unsatisfactory motion field. We propose the KVFC to add constraints to the remaining correspondences and eliminate outliers after prefiltering, given that sea-ice dynamic coherence.

1) Prefiltering by NNSR: NNSR utilizes the similarity of local feature descriptors to measure the distance between features [28]. It determines the closest (f_{closest}) and second closest (f_{second}) features and uses the equation g

$$\frac{D\left(f, f_{\text{closest}}\right)}{D\left(f, f_{\text{second}}\right)} \leq t_{\text{nnsr}} \tag{2}$$

where $D(\cdot)$ is a function calculating similarity. If the value of the distance ratio is less than the threshold t_{nnsr}, the correspondence is considered to be more discriminative and is regarded as an inlier.
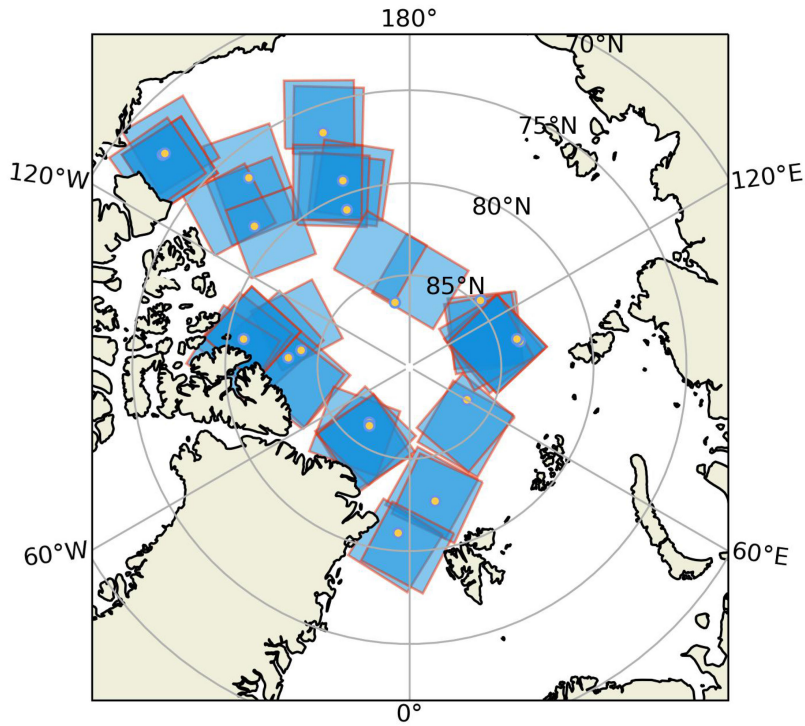
Fig. 2.   Spatial distribution of selected buoys and testing image pairs. The blue boxes show the Sentinel-1 images, and the yellow dots are the position of buoys.
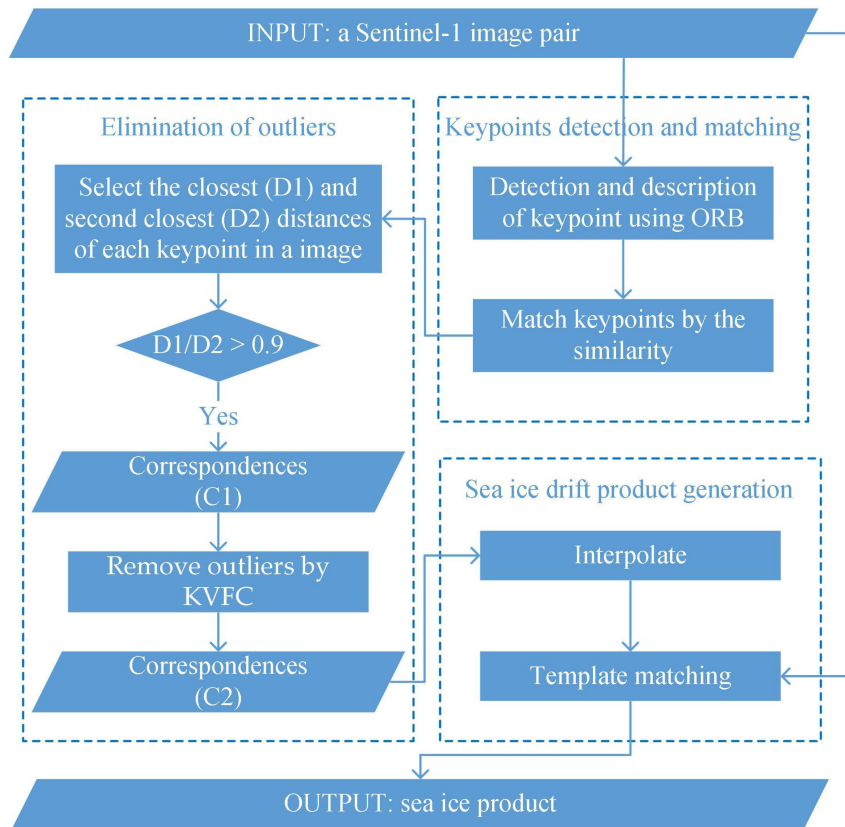

Fig. 3.   Flowchart of the entire sea-ice-tracking framework.

2) KVFC for removing outliers: The proposed KVFC is used to learn a motion field fitting for the remaining correspondences. Assume $M = \{(x_n, y_n)\}_{n=1}^{N}$ to be correspondences extracted from two images. In previous works [29], VFC is used to fit a vector field, which means to realize mapping, $f : U \rightarrow V$, where U and V are input space and output space, respectively. This assumes that the noise for inliers follows the Gaussian distribution with zero mean and uniform standard deviation σ and that the noise for outliers follows the uniform distribution of $\frac{1}{\alpha}$, where α is a constant. Thus, the model is

$$
\begin{aligned}
p(Y|X, \theta) &= \prod_{n=1}^{N} p(y_n|x_n, \theta) \\
&= \prod_{n=1}^{N} p_n \left(\frac{\gamma}{(2\pi\sigma)^{D/2}} e^{-\frac{\|y_n - f(x_n)\|}{2\sigma^2}} + \frac{1 - \gamma}{\alpha} \right)
\end{aligned}
\tag{3}
$$

where $\theta = \{f, \gamma, \sigma^2\}$, p_n is the GMM component, γ is a preassumed percentage of inliers, and D is the dimension of the output space.

In the traditional VFC, the value of p_n is 1. However, few inliers that cannot determine the overall motion trend can easily be eliminated. While they may deviate for the global motion, there should be a way to keep these inliers. Their local structures are still well preserved due to the coherence of the motion, which means that they can be given large weights of GMM components. In this way, as many inliers as possible are retained. p_n is updated to the following formula

$$
p_n = (a + b \cdot \Phi(s_n))
\tag{4}
$$

where s_n is the value derived from the local structure, $\Phi(\cdot)$ is a function that makes the variable has more complex transformations, and a and b are two constants.

We adopted the *K*-nearest-neighbors method to implement s_n, which is computed using the expression

$$
s_n = \frac{1}{K} \left(\sum_{q=1}^{N} \sum_{x_q \in N_{x_n}^{K}, y_q \in N_{y_n}^{K}} 1 \right)
\tag{5}
$$

where $N_{x_n}^{K}$ and $N_{y_n}^{K}$ are the *K*-nearest keypoints set of x_n and y_n, respectively.

A set of neighborhoods with sizes $K = \{(k_l)\}_{l=1}^{L}$ make the model more robust [39]. In order that the rate of change $\Phi(\cdot)$ is not large when s_n is closer to 0 or 1 and is large when s_n is close to $\frac{1}{2}$, $\Phi(\cdot)$ is defined as

$$
\Phi(x) = \frac{1}{1 + e^{-x}} .
\tag{6}
$$

The expectation–maximization [40] algorithm is used to solve the maximum likelihood function. At *E*-step, each diagonal element $p(\text{inlier}|x_n, \theta)$ in the diagonal matrix P is the probability of the correspondence being evaluated as an inlier. The element

is updated using the formula

$$
p(\text{inlier}|x_n, \theta^{\text{new}}) = \frac{\gamma e^{-\frac{\|y_n - f(x_n)\|^2}{2\sigma^2}}}{\gamma e^{-\frac{\|y_n - f(x_n)\|^2}{2\sigma^2}} + (1 - \gamma) \frac{(2\pi\sigma^2)^{D/2}}{\alpha}} .
\tag{7}
$$

At *M*-step, a coefficient matrix C and $f(\cdot)$ are estimated by

$$
\left(K_{\text{kernel}} + \lambda \sigma P^{-1} \right) C = Y
\tag{8}
$$

and

$$
f(x) = \sum_{n=1}^{N} k(x, x_n) c_n
\tag{9}
$$

where $C = (c_1^{\text{T}}, \ldots, c_N^{\text{T}})^{\text{T}}$, λ is a regularization parameter, K_{kernel} consists of $k(x_i, x_j) = e^{-\beta\|x_i - x_j\|_2}$. Finally, γ and σ^2 can be obtained by

$$
\gamma = \text{tr}(P) / N
\tag{10}
$$

and

$$
\sigma^2 = \frac{\text{tr}\left[(Y - f(X))^{\text{T}} P (Y - f(X)) \right]}{D \cdot \text{tr}(P)} .
\tag{11}
$$

C. Sea-Ice Drift Product Generation

Using the previous steps, good correspondences representing the motion vector of sea ice have been retained. However, these vectors are sparse and uneven and cannot directly generate sea-ice drift products. Muckenhuber *et al.* [33] recommend a combination of linear barycentric interpolation and pattern matching to generate the final sea-ice drift product. We referred to this method in this article.

In the linear barycentric interpolation, the keypoints are triangulated first. The triangle constructed from three neighboring keypoints are used to compute the motion of the position we are interested in.

The motion of sea ice is not a rigid body motion, and sea-ice drift vectors obtained by interpolation are only estimates. Therefore, small-scale adjustments are made through pattern matching. The normalized cross-correlation (NCC) [41], which is a type of pattern matching, is used, given by the expression

$$
\begin{aligned}
&R(x, y) \\
&= \frac{\sum_{x', y} (T_2(x', y') \cdot T_1(x + x', y + y'))}{\sqrt{\sum_{x', y} T_2(x', y')^2 \cdot \sum_{x', y} T_1(x + x', y + y')}}
\end{aligned}
\tag{12}
$$

where T_1 is the image needed to be matched; T_2 is the template; and, x, y, x', and y' represent the positions.

IV. RESULT

We first tested the performance of the proposed KVFC algorithm, as the validity of the proposed algorithm has to be first confirmed before it is applied to the sea-ice-tracking framework. Then, we focus on parameter tuning and the method's application in monitoring sea-ice drift. In the part of experiments, the HH polarization mode of SAR images was selected by default for analysis. The results are visualized for understanding and

TABLE II
PERFORMANCE OF NNSR WITH A THRESHOLD OF 0.7, RANSAC, GMS, LPM, VFC, AND KVFC USING DIFFERENT DETECTOR-DESCRIPTOR
COMBINATIONS ON THE THREE DATASETS

			NNSR	RANSAC	GMS	LPM	VFC	KVFC
Dataset I	SIFT	Precision	**75.00%**	55.13%	51.75%	55.36%	52.18%	62.63%
		Recall	5.15%	52.17%	17.89%	47.66%	52.24%	**60.91%**
		F-measure	8.92%	53.45%	23.69%	45.80%	51.85%	**61.17%**
		MCC	14.78%	52.03%	25.04%	46.37%	59.92%	**74.69%**
	ORB	Precision	**89.79%**	87.24%	76.34%	76.04%	69.14%	76.25%
		Recall	32.66%	50.53%	57.31%	71.66%	40.35%	**74.36%**
		F-measure	45.32%	58.96%	64.70%	73.34%	68.87%	**74.39%**
		MCC	42.75%	56.78%	57.28%	38.72%	83.97%	**88.84%**
Dataset II	SIFT	Precision	4.35%	4.64%	6.29%	17.62%	6.19%	**18.28%**
		Recall	0.03%	3.99%	2.88%	12.26%	13.74%	**25.70%**
		F-measure	0.07%	3.77%	3.70%	11.57%	6.97%	**20.46%**
		MCC	0.30%	2.16%	3.75%	12.23%	5.59%	**20.06%**
	ORB	Precision	39.79%	26.95%	42.13%	33.00%	31.79%	**44.15%**
		Recall	5.58%	7.15%	41.11%	16.19%	40.35%	**47.60%**
		F-measure	9.17%	9.69%	38.61%	20.57%	34.41%	**44.49%**
		MCC	12.45%	10.86%	37.95%	20.52%	33.89%	**44.15%**
Dataset III	SIFT	Precision	-	**99.63%**	99.24%	97.24%	97.56%	97.55%
		Recall	-	46.42%	48.35%	**97.45%**	87.15%	94.25%
		F-measure	-	61.32%	62.24%	**97.28%**	91.44%	95.63%
		MCC	-	50.73%	51.23%	**93.40%**	83.31%	91.04%
	ORB	Precision	-	**99.63%**	99.24%	97.24%	97.56%	97.55%
		Recall	-	46.42%	48.35%	**97.45%**	87.15%	94.25%
		F-measure	-	61.32%	62.24%	**97.28%**	91.44%	95.63%
		MCC	-	50.73%	51.23%	**93.40%**	83.31%	91.04%

The algorithm that reaches the optimum under the certain criteria is bolded.

observation. Before showing the results, we need to know the characteristics of the sea ice in the following three image pairs:

1) the thickness of the sea ice in Case 1 is thin, deforming easily, which makes its motion form complicated;
2) in Case 2, the sea ice is thick, but the speeds between some adjacent ice blocks vary;
3) the overall motion pattern is relatively simple in Case 3.

A. Performance of KVFC on Standard Datasets

Our KVFC was compared with state-of-the-art algorithms (NNSR, RANSAC [42], GMS [43], LPM [39], VFC) commonly used to eliminate outliers. We used *F*-measure and Matthews correlation coefficient (MCC) to evaluate the performance of KVFC. Different detector–descriptor combinations, such as SIFT and ORB, were applied to extract and describe features to further verify the robustness of algorithms.

Three datasets (i.e., Dataset I, Dataset II, and Dataset III) were used for testing. Since the homography matrix H was known except for the Dataset III, we could find the correct corresponding position of any keypoint detected in Dataset I. If the deviation is less than 10 pixels, the correspondence is regarded as an inlier. We also considered two different detector–descriptor combinations, SIFT and ORB, to test if similar results could be obtained.

Before our experiments, when $\alpha = 0.1$ and $K = \{4, 6, 8\}$, KVFC could achieve an excellent performance. The ORB parameters were based on the values from a previous study [24] and were used in further analysis. All other algorithms used the default parameters.

As shown by the performance evaluation results in Table II, the KVFC showed improvements from the VFC, achieving excellent results in precision and almost the best values in recall. For the *F*-measure taking into account both precision and recall, and the MCC comprehensively considering real samples and test samples, the KVFC was almost better than any other algorithm in the evaluation. This suggests that the proposed KVFC has great potential in the study of sea-ice drift. High values of *F*-measure and MCC mean that we have found more motion patterns and a higher proportion of inliers, which is very conducive to sea ice tracking scene.

B. Parameters Tuning of NNSR

The NNSR requires a threshold value. Since the threshold is expected to be larger than the standard, the range was set to (0.8, 1), with 0.1 step-size for screening. The threshold affects the number of remaining correspondences and the proportion of inliers. However, we encountered a problem when calculating the proportion of inliers: the sea ice images did not provide ground-truth labels for correspondences. Therefore, we assumed that the reference sea-ice motion pattern involved only simple translation. When the NNSR's threshold was 0.7, the speed that accounted for the largest number was correct, so the extracted correspondences could be divided into inliers and outliers. Fig. 4 illustrates the relationship between the three factors in Case 1. When the threshold is strict, a large number of correspondences are eliminated; in contrast, a loose threshold has a limited ability to increase the proportion of inliers. In order to achieve balance, 0.9 threshold was given to the threshold.

Fig. 5 shows the number of correspondences obtained from Case 1 at a certain offset in the horizontal direction u and vertical direction v and the results of the NNSR application.
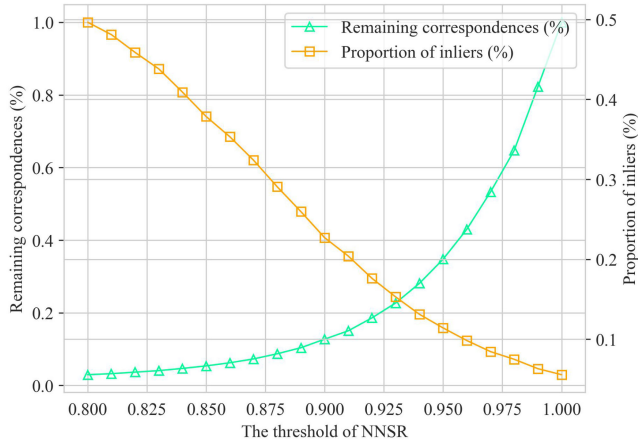
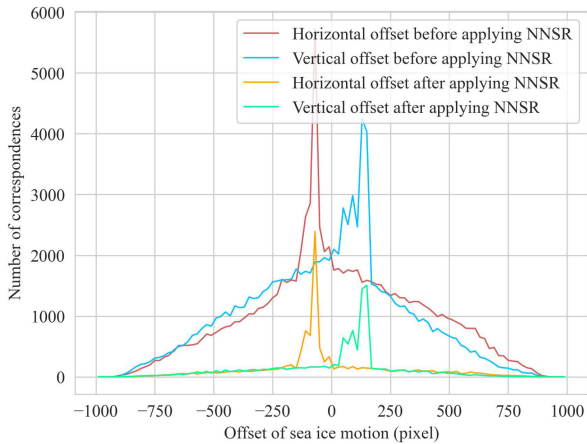Fig. 4. Proportions of remaining correspondences and inliers on different thresholds of NNSR in Case 1.

Fig. 5. Statistics of the number of correspondences of Case 1 at a certain offset in the horizontal and vertical directions.

We found that the offset of the latter in both directions is more concentrated, as expected.

C. Results on the Application of KVFC

We evaluated and compared the performance of the NNSR with a 0.7 threshold, VFC, and KVFC algorithms in removing residual outliers. Correspondences were labeled according to the processing method introduced in the section abovementioned. Fig. 6 presents the statistical information, which can be used as a reference for the performance evaluation. Based on the resulting box plots, the KVFC has the least isolated cases and outperforms the other two algorithms. Note that in Case 1, the precision of KVFC is slightly lower than that of VFC [see Fig. 6(a)]. This was because some motion patterns recognized by the KVFC were classified as outliers by previous steps, which was artificially confirmed by us.

NNSR with a strict threshold retains the least correspondences, and some do not conform to the law of sea-ice motion [for example, see Fig. 7(a)]. In addition, the distribution of outliers is scattered. We then compared in detail the VFC [see Fig. 7(b)] and the KVFC [see Fig. 7(c)]. In the figure, the subsets

TABLE III
COUNT THE NUMBER OF COMMON MOTION VECTORS AND INDIVIDUAL MOTION VECTORS ON HH AND HV

	Vector type	Number
	Common	3778
Case 1	Only HH	450
	Only HV	168
	Common	1217
Case 2	Only HH	437
	Only HV	1425
	Common	690
Case 3	Only HH	260
	Only HV	533

R1 and R2 show the outliers eliminated by VFC and KVFC. VFC is shown to retain serious erroneous motions in this area. In subset R3, KVFC was able to identify more inliers compared to VFC. The results suggest that on a wide baseline, VFC retains more inliers than the NNSR; however, outliers in spare areas are not easily eliminated. The KVFC can address this problem through structural information and is able to recognize inliers that VFC fails to find.

D. Comparison of HH and HV

The different polarizations have varying echoes on sea ice, resulting in differences in the displayed images. To better understand the spatial distribution of the filtered correspondences, we adopted the vector form to display extracted sparse drift under HH and HV Two vectors from different polarization are considered to be different motions if their deviation is outside ten pixels. Several visual results of sea ice images are presented in Fig. 8.

As presented in Table III, the HH and HV recognized common motion vectors in many identical positions. However, in some areas, only the HH was able to retain motion vectors; in other areas, HV achieved better results. This observation is similar to the findings of Komarov *et al.* [20]. We merged their vectors to get better results.

E. Validation

We utilized buoy data (i.e., time, latitude, and longitude information) from IABP to calculate the drift speed of sea ice and evaluated the algorithm's performance on the test set. Mean error (ME), root mean square error (RMSE), and absolute deviation of angle (ADOA) were used to measure the performance, and the summary of results is shown in Table IV. Each evaluation shows the advantages of KVFC over NNSR, which is due to our efforts to obtain more and more accurate matching vectors.

F. Efficiency

We designed an experiment to account for the computational efficiency of NNSR with a 0.7 threshold and the KVFC. The test set was inputted with 1000×1000 pixels to calculate the time consumed by each algorithm into a computer (2.90

	NNSR(0.7)	VFC	KVFC
Number	1017	4170	4228
Precision	98.03%	99.71%	99.69%
Recall	6.81%	28.39%	28.78%
F-measure	12.74%	44.20%	44.67%
MCC	23.72%	49.90%	50.25%

(a)

	NNSR(0.7)	VFC	KVFC
Number	162	1292	1654
Precision	83.95%	99.92%	100.00%
Recall	1.33%	12.60%	16.15%
F-measure	2.62%	22.38%	27.81%
MCC	9.70%	33.65%	38.18%

(b)

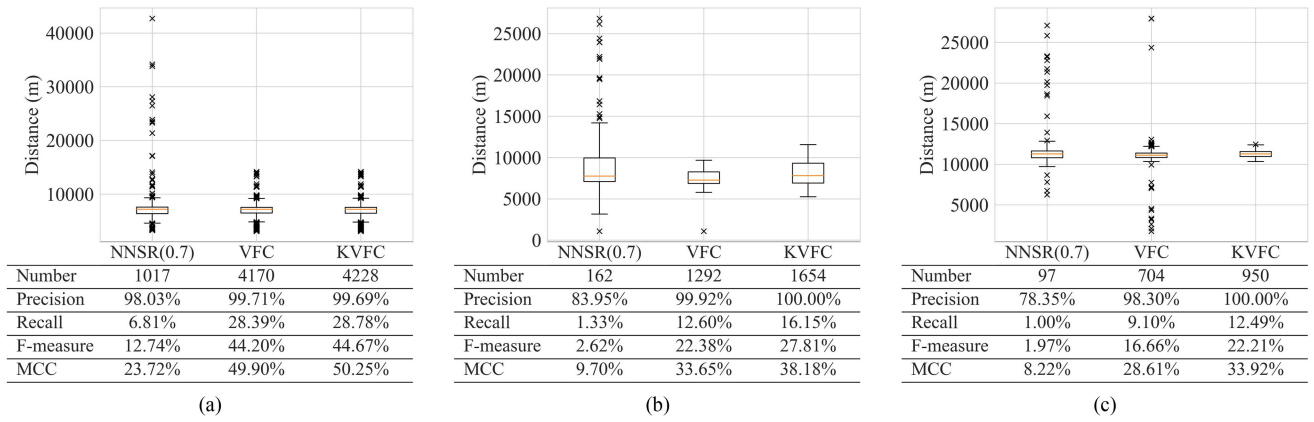|	NNSR(0.7)	VFC	KVFC
Number	97	704	950
Precision	78.35%	98.30%	100.00%
Recall	1.00%	9.10%	12.49%
F-measure	1.97%	16.66%	22.21%
MCC	8.22%	28.61%	33.92%

(c)

Fig. 6. Statistical information including isolated cases, the number of residual correspondences, precision, recall, *F*-measuer and MCC of applying different algorithms on three image pairs. (a)–(c) correspond to the statistics of Case 1, Case 2, and Case 3.
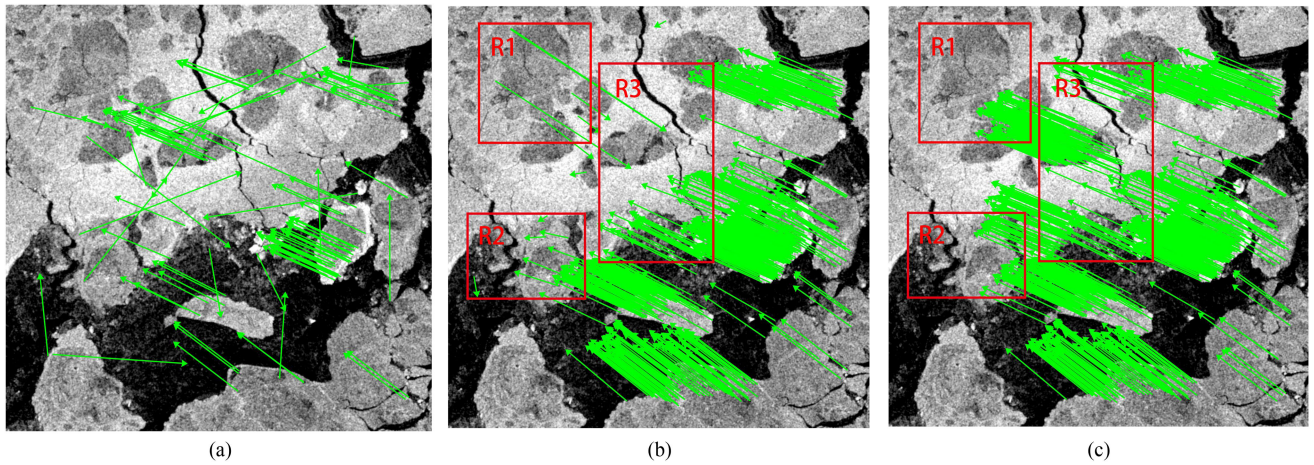

Fig. 7. Visual results of applying (a) NNSR with a 0.7 threshold, (b) VFC and (c) KVFC on Case 3. R1 and R2 delineate the outliers that are divided into inliers by VFC. R3 shows the advantage of KVFC to obtain inliers.
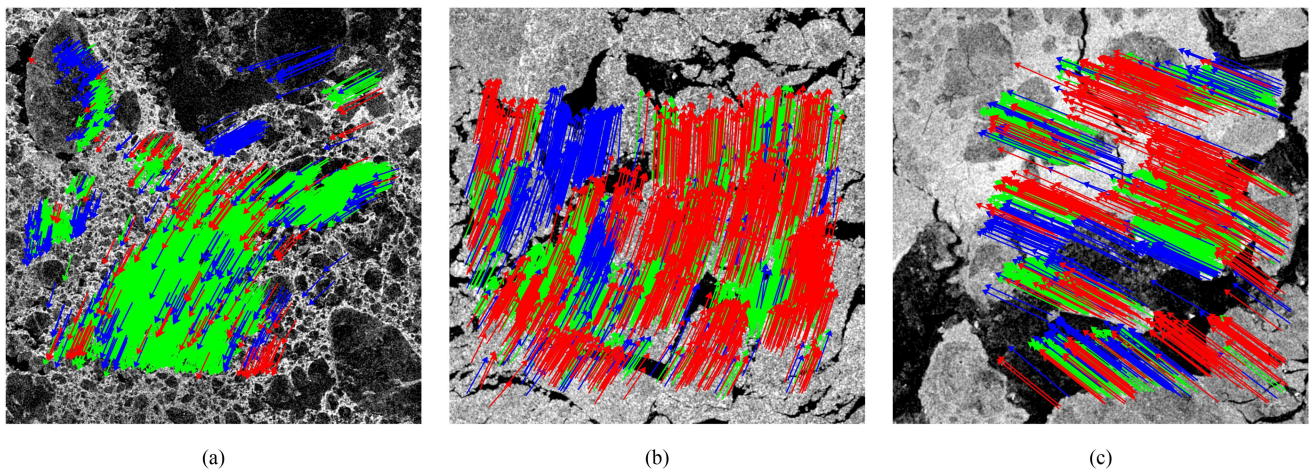

Fig. 8. Motion vector using KVFC on demonstration set. Red: motion pattern that only HV can recognize, blue: motion pattern that only HH can recognize, green: motion pattern recognized together.

TABLE IV
COMPARISON OF NNSR WITH A 0.7 THRESHOLD AND KVFC ON THE TEST SET

Algorithm	ME (cm/s)	RMSE (cm/s)	ADOA (°)	Average time (s)	Average number
NNSR (0.7)	0.407	1.817	10.318	34.589	2138.700
KVFC	-0.150	0.476	3.542	36.649	9453.400

GHz processor and 16 GB RAM). Since the two algorithms are implemented by Python or MATLAB, we only counted the execution time for each algorithm and added the time spent on the two platforms. The specific results (average time, average number) are reported in Table IV.

Note that it is normal that the NNSR with a 0.7 threshold is faster than the KVFC since the KVFC performs preliminary filtering of NNSR with a 0.9 threshold before execution. The proposed KVFC only takes a short extra time to obtain many times the number of correspondences than the NNSR with a 0.7 threshold guaranteeing matching performance.

V. DISCUSSION

Sea ice is often deformed due to extrusion, cracking, melting, and other factors, which means that monitoring its drift entails a study of nonrigid motion. The proposed KVFC is a modified version of the VFC, adding local information to learn a vector field that would help solve the tracking problem of sea ice. The main reasons why this strategy was adopted are as follows:

1) since sea-ice drift exhibits motion coherence, correspondences that do not conform to a vector field but cannot be filtered out by descriptor similarity should be removed;
2) due to the formation of leads and pressure zones by the sea-ice dynamics, some inliers may be slightly inconsistent with the vector field. Large weights should be assigned to their GMM components to be classified as inliers by the local correspondences;
3) outliers in some sparse areas can also be eliminated by local information. The improvement is applicable to datasets in other fields.

Before applying the KVFC directly to the feature tracking in sea-ice drift, we evaluated and compared its precision, recall, *F*-measure, MCC against other algorithms using three standard datasets. We used the correspondences extracted by SIFT and ORB to conduct experiments to assess the robustness of the algorithm. The results show that the KVFC performed better overall than the other algorithms. If the information of local structure is effectively used to assist feature tracking, the framework's performance would be greatly improved.

For sea ice tracking, correspondences from the Sentinel-1 images must be filtered. A strict threshold in the NNSR's screening is not conducive to obtaining enough correspondences. This situation is likely to occur in areas with few reference vectors. In the experiments, we selected a threshold of 0.9, which provided sufficient candidate vectors while increasing the percentage of inliers for subsequent processing. The KVFC only took a short amount of time to execute and was able to achieve good results. This suggests that we can obtain more correct vectors in vector field learning by increasing the probability that the inliers are correctly classified, which is particularly useful in monitoring sea-ice drift. Buoy data were used to verify that the KVFC improved the accuracy of sea ice tracking. It proves the effectiveness of obtaining more and more accurate matching vectors, especially obtaining new motion patterns in the sparse motion vector region.

While we were able to obtain a number of interesting results, there were several aspects can be improved in this study. Although rotational invariance is considered in the process of keypoint extraction, fine-grained matching using NCC does not have rotation invariance in the last step, which lead to a certain deviation within a small area. The feature texture of gray-level co-occurrence matrix [44] may be a good solution. Since the images are analyzed at the same scale down, it is not so necessary to consider the change of scaling compared with general tracking. Based on the prior knowledge, we can apply the relevant expert knowledge of sea ice movable range and the relationship between sea ice blocks in the tracking algorithm to further improve the rationality of the results.

VI. CONCLUSION

In this article, we proposed a novel algorithm for extracting sea-ice motion vectors in feature tracking in this article. The number of inliers extracted using the proposed KVFC are several times or even an order of magnitude more than those extracted by NNSR with a traditional standard threshold; the outliers in NNSR were also eliminated. A total of 20 pairs of Sentinel-1 image and buoys were used to verify our algorithm. When evaluating the algorithm performance, the KVFC had better results (ME: 0.150 cm/s, RMSE: 0.476 cm/s, ADOA: 3.542°) compared to the NNSR (ME: 0.407 cm/s, RMSE: 1.817 cm/s, ADOA: 10.318°). This means that the proposed algorithm has higher accuracy in determining velocity and direction than the traditional approach. The results indicate that the combination of the vector field and local information can improve the accuracy of sea-ice drift retrival.

REFERENCES

[1] R. Kwok, G. Spreen, and S. Pang, "Arctic sea ice circulation and drift speed: Decadal trends and ocean currents," *J. Geophys. Res. Oceans*, vol. 118, pp. 2408–2425, May 2013.
[2] E. Olason and D. Notz, "Drivers of variability in arctic sea-ice drift speed," *J. Geophys. Res. Oceans*, vol. 119, pp. 5755–5775, Sep. 2014.
[3] K. Nakata, K. I. Ohshima, S. Nihashi, N. Kimura, and T. Tamura, "Variability and ice production budget in the ross ice shelf polynya based on a simplified polynya model and satellite observations," *J. Geophys. Res. Oceans*, vol. 120, pp. 6234–6252, Sep. 2015.
[4] R. E. Jordan, E. L. Andreas, and A. P. Makshtas, "Heat budget of snow-covered sea ice at north pole 4," *J. Geophys. Res. Oceans*, vol. 104, pp. 7785–7806, Apr. 1999.
[5] G. Spreen, S. Kern, D. Stammer, and E. Hansen, "Fram strait sea ice volume export estimated between 2003 and 2008 from satellite data," *Geophys. Res. Lett.*, vol. 36, Oct. 2009, Art. no. L19502.

[6] R. Kwok, "Exchange of sea ice between the arctic ocean and the Canadian arctic archipelago," *Geophys. Res. Lett.*, vol. 33, Aug. 2006, Art. no. L16501.

[7] F. Girard-Ardhuin, "Enhanced arctic sea ice drift estimation merging radiometer and scatterometer data," *IEEE Trans. Geosci. Remote Sens.*, vol. 50, no. 7, pp. 2639–2648, Jul. 2012.

[8] S. Linow, T. Hollands, and W. Dierking, "An assessment of the reliability of sea-ice motion and deformation retrieval using SAR images," *Ann. Glaciol.*, vol. 56, pp. 229–234, Feb. 2015.

[9] T. Geldsetzer and J. J. Yackel, "Sea ice type and open water discrimination using dual co-polarized C-band SAR," *Can. J. Remote Sens.*, vol. 35, pp. 73–84, Jun. 2014.

[10] M. Kim, S. Li, and J. Martin, "Meso- and microscale sea-ice motion in the east siberian sea as determined from ERS-1 SAR data," *J. Glaciol.*, vol. 45, pp. 370–383, Jan. 2017.

[11] S. Bouillon and P. Rampal, "On producing sea ice deformation data sets from SAR-derived sea ice motion," *Cryosphere*, vol. 9, pp. 663–673, Apr. 2015.

[12] J. Kim, D. Kim, and B. J. Hwang, "Characterization of arctic sea ice thickness using high-resolution spaceborne polarimetric SAR data," *IEEE Trans. Geosci. Remote Sens.*, vol. 50, no. 1, pp. 13–22, Jan. 2012.

[13] Q. A. Holmes, D. R. Nuesch, and R. A. Shuchman, "Textural analysis and real-time classification of sea-ice types using digital SAR data," *IEEE Trans. Geosci. Remote Sens.*, vol. GE-22, no. 2, pp. 113–120, Mar. 2007.

[14] J. Gao and M. B. Lythe, "The maximum cross-correlation approach to detecting translational motions from sequential remote-sensing images," *Comput. Glaciol.*, vol. 22, pp. 525–534, Jun. 1996.

[15] M. Fily and DA Rothrock, "Sea ice tracking by nested correlations," *IEEE Trans. Geosci. Remote Sens.*, vol. GRS-25, no. 5, pp. 570–580, Sep. 1987.

[16] S. Gutiérrez and D. Long, "Optical flow and scale-space theory applied to sea-ice motion estimation in Antarctica," in *Proc. IEEE Int. Geosci. Remote Sens. Symp.*, 2003, pp. 2805–2807.

[17] M. Thomas, CA Geiger, and C. Kambhamettu, "High resolution (400m) motion characterization of sea ice using ERS-1 SAR imagery," *Cold Reg. Sci. Technol*, vol. 52, pp. 207–223, Apr. 2008.

[18] A. K. Liu, Y. Zhao, and S. Y. Wu, "Arctic sea ice drift from wavelet analysis of NSCAT and special sensor microwave imager data," *J. Geophys. Res. Oceans*, vol. 104, pp. 11529–11538, May 1999.

[19] M. Zhang, J. An, J. Zhang, D. Yu, and X. Lv, "Enhanced delaunay triangulation sea ice tracking algorithm with combining feature tracking and pattern matching," *Remote Sens.*, vol. 12, Feb. 2020, Art. no. 581.

[20] A. S. Komarov and D. G. Barber, "Sea ice motion tracking from sequential dual-polarization RADARSAT-2 images," *IEEE Trans. Geosci. Remote Sens .*, vol. 52, no. 1, pp. 121–136, Jan. 2013.

[21] R. Kwok and J. C. Curlander, "An ice-motion tracking system at the Alaska SAR facility," *IEEE J. Ocean. Eng.*, vol. 15, no. 1, pp. 44–54, Jan. 1990.

[22] A. Berg and L. Eriksson, "Investigation of a hybrid algorithm for sea ice drift measurements using synthetic aperture radar images," *IEEE Trans. Geosci. Remote Sens.*, vol. 52, no. 8, pp. 5023–5033, Aug. 2014.

[23] E. Rublee, V. Rabaud, K. Konolige, and G. R. Bradski, "ORB: An efficient alternative to SIFT or SURF," in *Proc. Int. Conf. Comput. Vis.*, 2011, pp. 2564–2571.

[24] S. Muckenhuber, A. A. Korosov, and S. Sandven, "Open-source feature-tracking algorithm for sea ice drift retrieval from sentinel-1 SAR imagery," *Cryosphere*, vol. 10, pp. 913–925, Apr. 2016.

[25] D. Demchev, V. Volkov, E. Kazakov, P. F. Alcantarilla, S. Sandven, and V. Khmeleva, "Sea ice drift tracking from sequential SAR images using Accelerated-KAZE features," *IEEE Trans. Geosci. Remote Sens.*, vol. 55, no. 4, pp. 5174–5184, Sep. 2017.

[26] M. S. Suganya and M. Bharathiraja, "Sea ice drift measurement using hybrid algorithm based on SAR images," *IEEE Trans. Geosci. Remote Sens.*, vol. 4, no. 2, pp. 371–376, Feb. 2015.

[27] K. Anton and R. Pierre, "A combination of feature tracking and pattern matching with optimal parametrization for sea ice drift retrieval from SAR data," *Remote Sens.*, vol. 9, Mar. 2017, Art. no. 258.

[28] D. G. Lowe, "Distinctive image features from scale-invariant keypoints," *Int. J. Comput. Vis.*, vol. 60, pp. 91–110, Jan. 2004.

[29] J. Ma, Z. Ji, J. Tian, A. L. Yuille, and Z. Tu, "Robust point matching via vector field consensus," *IEEE Trans. Image Process.*, vol. 23, no. 4, pp. 1706–1721, Apr. 2014.

[30] K. Mikolajczyk *et al.*, "A comparison of affine region detectors," *Int. J. Comput. Vis.*, vol. 65, pp. 43–72, Oct. 2005.

[31] D. Cabrini and H. N. Snavely, "Image matching using local symmetry features," in *Proc. IEEE Conf. Comput. Vis. Pattern Recognit.*, 2012, pp. 43–72.

[32] H. S. Wong, T. J. Chin, Y. Jin, and D. Suter, "Dynamic and hierarchical multi-structure geometric model fitting," in *Proc. Int. Conf. Comput. Vis.*, 2011, pp. 1044–1051.

[33] S. Muckenhuber and S. Sandven, "Open-source sea ice drift algorithm for sentinel-1 SAR imagery using a combination of feature tracking and pattern matching," *Cryosphere*, vol. 11, pp. 1835–1850, Aug. 2017.

[34] Ignatius G. Rigor, Pablo Clemente-Colon, and Ed Hudson, "The international arctic buoy programme (IABP): A cornerstone of the arctic observing network," in *Proc. IEEE OCEANS Conf.*, 2008, pp. 1–3.

[35] H. Bay, A. Ess, T. Tuytelaars, and L. T. Gool, "Speeded-Up robust features (SURF)," in *Proc. 9th Eur. Conf. Comput. Vis.*, 2006, pp. 404–417.

[36] E. Rosten and T. Drummond, "Machine learning for very high-speed corner detection," in *Proc. 9th Eur. Conf. Comput. Vis., Proc., Part I*, 2006, pp. 430–443.

[37] C. Harris and M. Stephens, "A combined corner and edge detector," in *Proc. Alvey Vis. Conf.*, 1988, pp. 147–151.

[38] M. Calonder, V. Lepetit, C. Strecha, and P. Fua, "BRIEF: Binary robust independent elementary features," in *Proc. Eur. Conf. Comput. Vis.*, 2010, pp. 778–792.

[39] J. Ma, J. Zhao, J. Jiang, Z. Huabing, and G. Xiaojie, "Locality preserving matching," *Int. J. Comput. Vis.*, vol. 127, pp. 512–531, 2019.

[40] A. P. Dempster, N. M. Laird, and D. B. Rubin, "Maximum likelihood from incomplete data via the EM algorithm," *J. Roy. Statist. Soc.*, vol. 39, pp. 1–38, 1977.

[41] T. Hollands, *Motion Tracking of Sea Ice with SAR Satellite Data*. Bremen, Germany: Universität Bremen, 2012.

[42] M. A. Fischler and R. C. Bolles, "Random sample consensus: A paradigm for model fitting with applications to image analysis and automated cartography," *Commun. ACM*, vol. 24, pp. 381–395, 1981.

[43] J. Bian, W.-Y. Lin, Y. Matsushita, S.-K. Yeung, T.-D. Nguyen, and M.-M. Cheng, "GMS: Grid-based motion statistics for fast, ultra-robust feature correspondences," in *Proc. IEEE Conf. Comput. Vis. Pattern Recognit.*, 2017, pp. 2828–2837.

[44] R. M. Haralick and K. Shanmugam, "Textural features for image classification," *IEEE Trans. Syst., Man, Cybern.*, vol. SMC-3, no. 6, pp. 610–621, Nov. 1973.
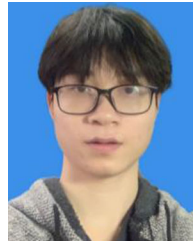
Bin He received the B.S. degree in software engineering in 2016 from Wuhan University, Wuhan, China, where he is currently working toward the master's degree in cartography and geographic information engineering with the Chinese Antarctic Center of Surveying and Mapping.

His research interests include artificial intelligence and remote sensing of sea ice.

Xi Zhao received the Ph.D. degree in earth observation science from the Faculty of Geo-Information Science and Earth Observation (ITC), University of Twente, Enschede, The Netherlands, in 2012.

From 2012 to 2021, she was an Associate Professor with the Chinese Antarctic Center of Surveying and Mapping, Wuhan University, Wuhan, China. Since September 2021, she has been an Associate Professor with the School of Geospatial Engineering and Science, Sun Yat-Sen University, Zhuhai, China. Her research interest is sea ice remote sensing and uncertainty of spatial data.

Ying Chen received the B.S. degree in geographic information science from Changan University, Xi'an, China, in 2014. She is currently working toward the Ph.D. degree in cartography and geographic information engineering with the Chinese Antarctic Center of Surveying and Mapping, Wuhan University, Wuhan, China.

Her research interests include remote sensing of sea ice.

Chuang Liu received the B.S. degree in geographic information science from Huazhong Agricultural University, Wuhan, China, in 2019. He is currently working toward the master's degree in cartography and geographic information engineering with the Chinese Antarctic Center of Surveying and Mapping, Wuhan University, Wuhan, China.

His research interests include machine learning and synthetic aperture radar.

Xiaoping Pang received the Ph.D. degree in solid geophysics from Wuhan University, Wuhan, China, in 2007.

She is currently a Professor and the Deputy Director of the Chinese Antarctic Center of Surveying and Mapping, Wuhan University. She has made three scientific investigations to the north and south poles. Her research interests include remote sensing of sea ice, dynamic simulation of polar ice and snow environment, digital mapping, and geographic information visualization.